This article was downloaded by: [DLR-Bibliotheken]
On: 18 July 2012, At: 00:15
Publisher: Taylor & Francis
Informa Ltd Registered in England and Wales Registered Number: 1072954 Registered office: Mortimer House, 37-41 Mortimer Street, London W1T 3JH, UK

Vehicle System Dynamics: International Journal of Vehicle Mechanics and Mobility

Publication details, including instructions for authors and subscription information:
http://www.tandfonline.com/loi/nvsd20

Refining the modelling of vehicle-track interaction

Ingo Kaiser [a]

[a] German Aerospace Center (DLR) Oberpfaffenhofen, Institute of Robotics and Mechatronics, Muenchner Strasse 20, D-82234, Wessling, Germany

Version of record first published: 16 Jul 2012

To cite this article: Ingo Kaiser (2012): Refining the modelling of vehicle-track interaction, Vehicle System Dynamics: International Journal of Vehicle Mechanics and Mobility, 50:sup1, 229-243

To link to this article: http://dx.doi.org/10.1080/00423114.2012.671948

PLEASE SCROLL DOWN FOR ARTICLE

Full terms and conditions of use: http://www.tandfonline.com/page/terms-and-conditions

This article may be used for research, teaching, and private study purposes. Any substantial or systematic reproduction, redistribution, reselling, loan, sub-licensing, systematic supply, or distribution in any form to anyone is expressly forbidden.

The publisher does not give any warranty express or implied or make any representation that the contents will be complete or accurate or up to date. The accuracy of any instructions, formulae, and drug doses should be independently verified with primary sources. The publisher shall not be liable for any loss, actions, claims, proceedings, demand, or costs or damages whatsoever or howsoever caused arising directly or indirectly in connection with or arising out of the use of this material.

Vehicle System Dynamics
Vol. 50, Supplement, 2012, 229–243

Taylor & Francis
Taylor & Francis Group

Refining the modelling of vehicle–track interaction

Ingo Kaiser*

German Aerospace Center (DLR) Oberpfaffenhofen, Institute of Robotics and Mechatronics, Muenchner Strasse 20, D-82234 Wessling, Germany

(*Received 31 October 2011; final version received 27 February 2012*)

An enhanced model of a passenger coach running on a straight track is developed. This model includes wheelsets modelled as rotating flexible bodies, a track consisting of flexible rails supported on discrete sleepers and wheel–rail contact modules, which can describe non-elliptic contact patches based on a boundary element method (BEM). For the scenarios of undisturbed centred running and permanent hunting, the impact of the structural deformations of the wheelsets and the rails on the stress distribution in the wheel–rail contact is investigated.

Keywords: vehicle–track interaction; flexible wheelset; flexible track; non-elliptic wheel–rail contact

Downloaded by [DLR-Bibliotheken] at 00:15 18 July 2012

1. Introduction and motivation

The modelling of railway vehicles as multi-body systems (MBS) is a well-established technology today. In MBS modelling, the real system is modelled by a combination of rigid bodies having a mass and force elements acting between the bodies. The motions of the bodies are determined by joints and constraints. Together with the modelling of the wheel–rail contact based on the Hertzian theory, this forms a powerful tool, which covers a wide range of dynamical problems related to railway vehicles. However, there are still some problems related to the vehicle–track interaction, which require an enhancement of the modelling described above: For noise investigations structural vibrations of the wheelsets and the rails are essential, which requires modelling of these components as flexible bodies. To analyse the wear occurring in the wheel–rail contact, a detailed contact model is needed, since wear can only occur in the actual contact area. Of course, these problems are linked with each other, e.g. due to the influence of structural deformations on the contact. This also rises the question, what kind of influence the deformations of wheelsets and rails have on the running behaviour, which is determined by the contact forces.

In this work, a refined vehicle–track model including the structural dynamics of wheelsets and rails and a detailed contact model will be developed. The influence of the refinements on the running behaviour will be investigated for two idealised scenarios. This also serves as a plausibility check of the refined model.

*Email: ingo.kaiser@dlr.de

ISSN 0042-3114 print/ISSN 1744-5159 online
© 2012 Taylor & Francis
http://dx.doi.org/10.1080/00423114.2012.671948
http://www.tandfonline.com

2. Vehicle–track model

The vehicle–track model describes a railway passenger coach running on a straight track. An overview of the bodies, of which the system is composed, is given in Figure 1. The carbody, the bogie frames and the bolsters are modelled as rigid bodies. Each bogie frame and each wheelset can perform all six rigid body motions. The carbody has five degrees of freedom, since a constant running speed v_0 is set for its longitudinal motion. The bolsters can only perform yaw motions relative to the carbody. The bogie frames are connected to the wheelsets and to the bolsters by linear springs and dampers. A yaw damping using dry friction acts between each bolster and the carbody. The parameters of the vehicle model are taken from [1,2].

Since the wheelsets, the track and the wheel–rail contacts are the key components for the vehicle–track interaction, the models for these components are refined compared to the 'standard modelling' provided by commercial MBS tools. Selected aspects concerning the refined modelling will be presented in the following sections.

Downloaded by [DLR-Bibliotheken] at 00:15 18 July 2012

2.1. *Flexible wheelset*

For the description of a flexible body, a relative formulation is used. Here, the motion of a particle is described by superposing the motion of the undeformed structure with the deformation. The so-called rigid body motions are expressed by the vector $\mathbf{r}_{\mathsf{R}}^{\mathcal{I}}$, describing the current position of the reference point R and the matrix $\mathbf{A}^{\mathcal{I}\mathcal{B}}$, indicating the rotation of a frame $\mathcal{B}$ related to the body relative to the initial frame $\mathcal{I}$. The position of the particle in the undeformed state is represented by the vector $\mathbf{x}^{\mathcal{B}}$. The deformation field depending on the time t and on the reference position of the particle, in this case $\mathbf{x}^{\mathcal{B}}$, is represented by the vector $\mathbf{w}^{\mathcal{B}}$. An overview of the kinematics is displayed in Figure 2. In total, the position of the particle is given by

$$\mathbf{r}_{\mathsf{P}}^{\mathcal{I}} = \mathbf{r}_{\mathsf{R}}^{\mathcal{I}}(t) + \mathbf{A}^{\mathcal{I}\mathcal{B}}(t)[\mathbf{x}^{\mathcal{B}} + \mathbf{w}^{\mathcal{B}}(\mathbf{x}^{\mathcal{B}}, t)]. \tag{1}$$

In the following, the dependency of the expressions on time will not always be displayed explicitly for the sake of brevity, once the expressions have been introduced. The main difficulty is the overturning motion of the wheelset and the wheel–rail forces moving around the wheels. Thereby, the considered reference point $\mathbf{x}^{\mathcal{B}}$ changes permanently due to the time-variant angle $\phi = \phi(t)$. If the deformation $\mathbf{w}^{\mathcal{B}}(\mathbf{x}^{\mathcal{B}}, t)$ is expressed by a modal synthesis, the

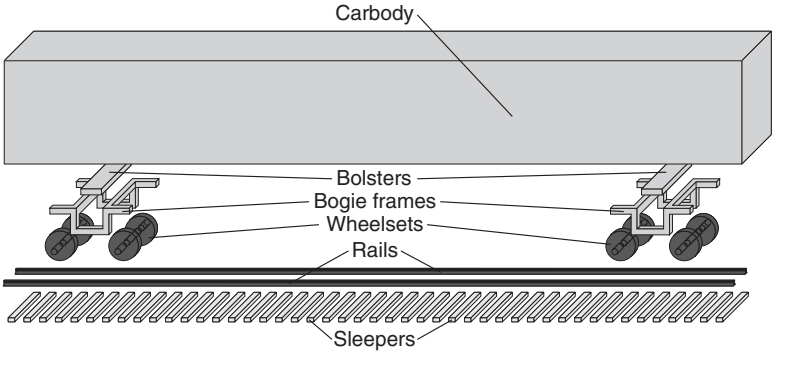

Figure 1. Bodies of the vehicle–track system; dark bodies are modelled as flexible bodies.

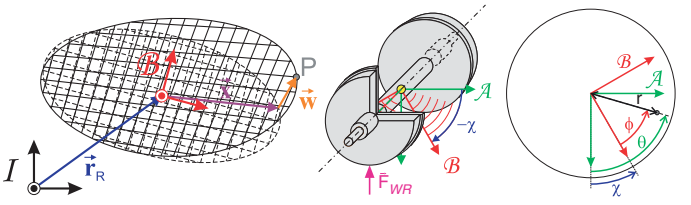

Figure 2. Kinematics for a particle of a flexible body (left), body-fixed frame $\mathcal{B}$ and axle-fixed frame $\mathcal{A}$ (right).

modal coefficients $\mathbf{w}_i^{\mathcal{B}}$ depend on time:

$$\mathbf{w}^{\mathcal{B}}(\mathbf{x}^{\mathcal{B}}(t),t) = \sum_i \mathbf{w}_i^{\mathcal{B}}(\mathbf{x}^{\mathcal{B}}(t))q_i(t) = \sum_i \mathbf{w}_i^{\mathcal{B}}(t)q_i(t). \tag{2}$$

To avoid any misunderstandings, it should be pointed out that the dependence of the reference point does not describe any velocity, but expresses that with varying time another particle indicated by another value of ϕ is observed. Therefore, the relative velocity of the particle observed in the body-fixed frame $\mathcal{B}$ is derived as

$$\mathbf{r}_{\mathrm{RP}}^{\mathcal{B}} = \mathbf{x}^{\mathcal{B}}(t) + \sum_i \mathbf{w}_i^{\mathcal{B}}(\mathbf{x}^{\mathcal{B}}(t))q_i(t) \Rightarrow \mathbf{v}_{\mathrm{RP}}^{\mathcal{B}} = \sum_i \mathbf{w}_i^{\mathcal{B}}(\mathbf{x}^{\mathcal{B}}(t))\dot{q}_i(t). \tag{3}$$

To solve the problem, a new axle-fixed frame $\mathcal{A}$ is introduced, as shown in Figure 2. This frame performs all the motions of the body-fixed frame $\mathcal{B}$ except the overturning motion, so that in frame $\mathcal{A}$ the vector $\mathbf{x}^{\mathcal{A}}$ indicating the particle, on which the wheel–rail forces act, is constant. In the case of the wheelset, the transformation matrix $\mathbf{A}^{\mathcal{AB}} = \mathbf{A}_2(\chi)$ describes a rotation around the 2-axis with the overturning angle χ. Here and in the following consideration, the matrix $\mathbf{A}_j(\alpha)$ describes a rotation around the j-axis with the angle α. The matrix $\mathbf{A}^{\mathcal{IB}}$ is composed of a sequence of rotations with the yaw angle ψ, the roll angle φ and the overturning angle χ, in which the rotation with χ has to be the last one in the sequence. Then, the matrix $\mathbf{A}^{\mathcal{IB}}$ is split up to

$$\mathbf{A}^{\mathcal{IB}} = \underbrace{\mathbf{A}_3(\psi)\mathbf{A}_1(\varphi)}_{\mathbf{A}^{\mathcal{IA}}}\underbrace{\mathbf{A}_2(\chi)}_{\mathbf{A}^{\mathcal{AB}}}. \tag{4}$$

Since the wheelset is a rotational symmetric structure, the use of cylindrical coordinates is obvious, whereas r, ϕ and y are the radial coordinate, the polar angle and the axial coordinate, respectively. Furthermore, the deformations U, V and W describing displacements in cartesian coordinates are expressed by the radial deformation R, the tangential deformation T and the axial deformation V. Thus, the following relation can be derived:

$$\begin{bmatrix} x \\ y \\ z \end{bmatrix} + \begin{bmatrix} U(r,\phi,y,t) \\ V(r,\phi,y,t) \\ W(r,\phi,y,t) \end{bmatrix} = \begin{bmatrix} \cos\phi & 0 & \sin\phi \\ 0 & 1 & 0 \\ -\sin\phi & 0 & \cos\phi \end{bmatrix} \left(\begin{bmatrix} 0 \\ y \\ r \end{bmatrix} + \begin{bmatrix} T(r,\phi,y,t) \\ V(r,\phi,y,t) \\ R(r,\phi,y,t) \end{bmatrix} \right) \tag{5}$$

$$\Rightarrow \mathbf{x}^{\mathcal{B}}(r,\phi,y) + \mathbf{w}^{\mathcal{B}}(r,\phi,y,t) = \mathbf{A}_2(\phi)(\mathbf{c}(r,y) + \mathbf{u}(r,\phi,y,t)). \tag{6}$$

It is obvious to express the distribution of the deformations by a Fourier series. For the description of the deformation field, a modal synthesis is used. Here, each shape function has one and only one periodicity $k_i \in \mathbb{Z}$ and for $k_i \neq 0$ two orthogonal shape functions having

Downloaded by [DLR-Bibliotheken] at 00:15 18 July 2012

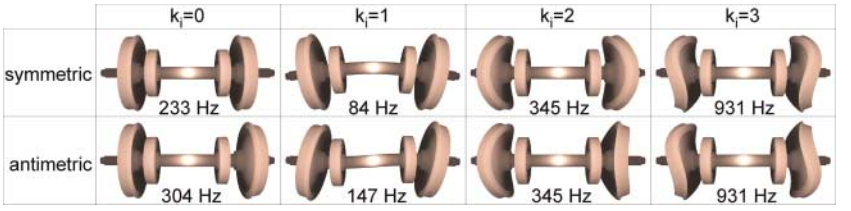

Figure 3. Eigenmodes of the wheelset.

the following structure are used:

$$\mathbf{u}(r,\phi,y,t) = \sum_i [\mathbf{u}_{i,1}(r,\phi,y)q_{i,1}(t) + \mathbf{u}_{i,2}(r,\phi,y)q_{i,2}(t)], \tag{7}$$

$$\mathbf{u}_{i,1}(r,\phi,y) = \mathbf{u}_{i,A}(r,y)\cos(k_i\phi) + \mathbf{u}_{i,B}(r,y)\sin(k_i\phi), \tag{8}$$

$$\mathbf{u}_{i,2}(r,\phi,y) = \mathbf{u}_{i,A}(r,y)\sin(k_i\phi) - \mathbf{u}_{i,B}(r,y)\cos(k_i\phi). \tag{9}$$

For $k_i = 0$, rotational symmetric modes having no spatial orientation occur. Thereby, no double, but only single eigenmodes belonging to each eigenfrequency exist. The second modal coordinate is therefore set to $q_{i,2} \equiv 0$. Some examples of eigenmodes having different periodicities k_i are displayed in Figure 3. It can be shown, that the eigenmodes of a rotational symmetric structure can be expressed in the form of (8) and (9). For a rotational symmetric structure, the shear modulus $G = G(r,y)$, Poisson's ratio $\nu = \nu(r,y)$ and the density $\rho = \rho(r,y)$ are independent of the angle ϕ. Then, the expressions $\mathbf{w} = \mathbf{A}_2(\phi)\mathbf{u}_{i,1}(r,\phi,y)\cos(\omega_i t)$ and $\mathbf{w} = \mathbf{A}_2(\phi)\mathbf{u}_{i,2}(r,\phi,y)\cos(\omega_i t)$ are solutions of Navier's equation for a linear three-dimensional linearly elastic continuum, e.g. given in [3]:

$$G\left[\Delta\mathbf{w} + \frac{1}{1-2\nu}\mathbf{grad}\,\mathrm{div}\,\mathbf{w}\right] = \rho\ddot{\mathbf{w}}. \tag{10}$$

Here, Δ indicates the Laplace operator. The current position of the particle described in the axle-fixed frame $\mathcal{A}$ is obtained by the transformation:

$$\begin{aligned}\mathbf{x}^{\mathcal{A}}(r,\phi,y) + \mathbf{w}^{\mathcal{A}}(r,\phi,y,t) &= \mathbf{A}^{\mathcal{A}\mathcal{B}}[\mathbf{x}^{\mathcal{B}}(r,\phi,y) + \mathbf{w}^{\mathcal{B}}(r,\phi,y,t)] \\ &= \mathbf{A}_2(\chi)\mathbf{A}_2(\phi)[\mathbf{c}(r,y) + \mathbf{u}(r,\phi,y,t)].\end{aligned} \tag{11}$$

By combining the matrices the new angle θ used in the axle-fixed frame $\mathcal{A}$ is defined, as displayed in Figure 2:

$$\mathbf{A}_2(\chi)\mathbf{A}_2(\phi) = \mathbf{A}_2(\chi+\phi) = \mathbf{A}_2(\theta) \Rightarrow \theta = \chi + \phi \Leftrightarrow \phi = \theta - \chi. \tag{12}$$

It is important to note that the angle θ does not indicate a particle, but a certain location. This has to be taken into account for derivatives with respect to time. By inserting the theorems:

$$\sin(k_i\phi) = \sin(k_i(\theta-\chi)) = \sin(k_i\theta)\cos(k_i\chi) - \cos(k_i\theta)\sin(k_i\chi), \tag{13}$$

$$\cos(k_i\phi) = \cos(k_i\,(\theta-\chi)) = \cos(k_i\theta)\cos(k_i\chi) + \sin(k_i\theta)\sin(k_i\chi) \tag{14}$$

Downloaded by [DLR-Bibliotheken] at 00:15 18 July 2012

into the shape functions $\mathbf{u}_{i,1}(r,\phi,y)$ and $\mathbf{u}_{i,2}(r,\phi,y)$ and factoring out the terms $\cos(k_i\theta)$ and $\sin(k_i\theta)$, the following expressions are obtained:

$$\begin{aligned}\mathbf{u}_{i,1}(r,\phi,y) &= [\mathbf{u}_{i,A}(r,y)\cos(k_i\theta) + \mathbf{u}_{i,B}(r,y)\sin(k_i\theta)]\cos(k_i\chi)\\ &\quad + [\mathbf{u}_{i,A}(r,y)\sin(k_i\theta) - \mathbf{u}_{i,B}(r,y)\cos(k_i\theta)]\sin(k_i\chi)\\ &= \mathbf{u}_{i,1}(r,\theta,y)\cos(k_i\chi) + \mathbf{u}_{i,2}(r,\theta,y)\sin(k_i\chi), \qquad (15)\\ \mathbf{u}_{i,2}(r,\phi,y) &= [\mathbf{u}_{i,A}(r,y)\sin(k_i\theta) - \mathbf{u}_{i,B}(r,y)\cos(k_i\theta)]\cos(k_i\chi)\\ &\quad - [\mathbf{u}_{i,A}(r,y)\cos(k_i\theta) + \mathbf{u}_{i,B}(r,y)\sin(k_i\theta)]\sin(k_i\chi)\\ &= \mathbf{u}_{i,2}(r,\theta,y)\cos(k_i\chi) - \mathbf{u}_{i,1}(r,\theta,y)\sin(k_i\chi). \qquad (16)\end{aligned}$$

By transforming these relations into the following:

$$\mathbf{u}_{i,1}(r,\theta,y) = \mathbf{u}_{i,1}(r,\phi,y)\cos(k_i\chi) - \mathbf{u}_{i,2}(r,\phi,y)\sin(k_i\chi), \qquad (17)$$

$$\mathbf{u}_{i,2}(r,\theta,y) = \mathbf{u}_{i,2}(r,\phi,y)\cos(k_i\chi) + \mathbf{u}_{i,1}(r,\phi,y)\sin(k_i\chi) \qquad (18)$$

the basic idea can be seen: The shape functions $\mathbf{u}_{i,1}(r,\theta,y)$ and $\mathbf{u}_{i,2}(r,\theta,y)$ described in the axle-fixed frame $\mathcal{A}$ are expressed by linear combinations of the shape functions $\mathbf{u}_{i,1}(r,\phi,y)$ and $\mathbf{u}_{i,2}(r,\phi,y)$ described in the body-fixed frame $\mathcal{B}$. Inserting the relations between the shape functions described in frame $\mathcal{B}$ and those described in frame $\mathcal{A}$ and rearranging the terms leads to the following expression:

$$\begin{aligned}\mathbf{A}^{\mathcal{AB}}[\mathbf{w}^{\mathcal{B}}_{i,1}(r,\phi,y)q_{i,1} + \mathbf{w}^{\mathcal{B}}_{i,2}(r,\phi,y)q_{i,2}] &= \mathbf{A}_2(\chi)\mathbf{A}_2(\phi)\mathbf{u}_{i,1}(r,\phi,y)q_{i,1}\\ &\quad + \mathbf{A}_2(\chi)\mathbf{A}_2(\phi)\mathbf{u}_{i,2}(r,\phi,y)q_{i,2}\\ &= \underbrace{\mathbf{A}_2(\theta)\mathbf{u}_{i,1}(r,\theta,y)}_{\mathbf{w}^{\mathcal{A}}_{i,1}(r,\theta,y)}\underbrace{[\cos(k_i\chi)q_{i,1} - \sin(k_i\chi)q_{i,2}]}_{Q_{i,1}}\\ &\quad + \underbrace{\mathbf{A}_2(\theta)\mathbf{u}_{i,2}(r,\theta,y)}_{\mathbf{w}^{\mathcal{A}}_{i,2}(r,\theta,y)}\underbrace{[\sin(k_i\chi)q_{i,1} + \cos(k_i\chi)q_{i,2}]}_{Q_{i,2}}.\end{aligned} \qquad (19)$$

Here, the new modal coordinates $Q_{i,1}$ and $Q_{i,2}$ used in frame $\mathcal{A}$ are defined. Since the modal functions $\mathbf{u}_{i,1}(r,\theta,y)$ and $\mathbf{u}_{i,2}(r,\theta,y)$ contain the angle θ, this has to be taken into account for the derivative with respect to time:

$$\begin{aligned}\mathbf{u}_{i,1}(r,\phi,y)\dot{q}_{i,1} + \mathbf{u}_{i,2}(r,\phi,y)\dot{q}_{i,2} &= \frac{\partial\mathbf{u}_{i,1}(r,\theta,y)}{\partial\theta}\frac{\mathrm{d}\theta}{\mathrm{d}t}Q_{i,1} + \mathbf{u}_{i,1}(r,\theta,y)\dot{Q}_{i,1}\\ &\quad + \frac{\partial\mathbf{u}_{i,2}(r,\theta,y)}{\partial\theta}\frac{\mathrm{d}\theta}{\mathrm{d}t}Q_{i,2} + \mathbf{u}_{i,2}(r,\theta,y)\dot{Q}_{i,2}\\ &= \mathbf{u}_{i,1}(r,\theta,y)[\dot{Q}_{i,1} + k_i\dot{\chi}Q_{i,2}] + \mathbf{u}_{i,2}(r,\theta,y)[\dot{Q}_{i,2} - k_i\dot{\chi}Q_{i,1}].\end{aligned} \qquad (20)$$

The relations $\partial\mathbf{u}_{i,1}(r,\theta,y)/\partial\theta = -k_i\mathbf{u}_{i,2}(r,\theta,y)$ and $\partial\mathbf{u}_{i,2}(r,\theta,y)/\partial\theta = k_i\mathbf{u}_{i,1}(r,\theta,y)$, which are used here, are derived from Equations (8) and (9). Finally, the position of the particle can

Downloaded by [DLR-Bibliotheken] at 00:15 18 July 2012

be described by the following expressions:

$$\mathbf{r}_{\mathsf{P}}^{\mathcal{I}} = \mathbf{r}_{\mathsf{R}}^{\mathcal{I}} + \mathbf{A}^{\mathcal{IB}}[\mathbf{x}^{\mathcal{B}}(r,\phi(t),y) + \sum_i [\mathbf{w}_{i,1}^{\mathcal{B}}(r,\phi(t),y)q_{i,1} + \mathbf{w}_{i,2}^{\mathcal{B}}(r,\phi(t),y)q_{i,2}]] \tag{21}$$

$$= \mathbf{r}_{\mathsf{R}}^{\mathcal{I}} + \mathbf{A}^{\mathcal{IA}}[\mathbf{x}^{\mathcal{A}}(r,\theta,y) + \sum_i [\mathbf{w}_{i,1}^{\mathcal{A}}(r,\theta,y)Q_{i,1} + \mathbf{w}_{i,2}^{\mathcal{A}}(r,\theta,y)Q_{i,2}]]. \tag{22}$$

In the second expression, the modal coefficients $\mathbf{w}_{i,1}^{\mathcal{A}}(r,\theta,y)$ and $\mathbf{w}_{i,2}^{\mathcal{A}}(r,\theta,y)$ are constant. Furthermore, the large overturning angle χ, which was originally contained in the matrix $\mathbf{A}^{\mathcal{IB}}$ has been eliminated. By considering the shape functions in (21) and (22), it can be seen that the shape functions differ only by the polar angle. Since ϕ and θ are defined for the same interval, namely $[0, 2\pi]$, the coefficients obtained by integrating products of the shape functions for all mass particles of the structure remain unchanged. Therefore, the problem of the overturning structure with moving forces is solved by a comparatively simple transformation of the modal coordinates. Further details and extensions can be found in [4].

2.2. *Track model*

In this work, a structural model of the track is used, which is based on the model developed by Ripke [5]. This model consists of two flexible rails supported by discrete rigid sleepers. The sleepers can perform all six rigid body motions and are connected to the rails and to the fixed ground by linear springs and dampers. An overview of the track model in given in Figure 4. For a comparison, a simple track model taken from [6] is used, which is also depicted in Figure 4. This model consists of a rigid body, which is connected to the fixed ground by springs and dampers and can perform lateral, vertical and roll motions. Each wheelset is supported by such a model, which moves along the track.

A general problem related to the modelling of the track is the large track length: By running with $v_0 = 180\,\text{km/h}$ during a time interval of $\Delta t = 10\,\text{s}$, the vehicle covers a distance of $v_0 \cdot \Delta t = 500\,\text{m}$. A track model of such a length would require a very high numerical effort. If only the reaction of the track is of interest, i.e. the motions of the rail head under the wheels, this problem can be reduced: In [5] a shorter track model is used, whereas the boundary conditions at the ends of the rails are set to be equal. Thereby, the track model forms a ring, so that the vehicle never reaches the end of the track. However, the curvature of the ring is neglected, i.e. the topology of the structural dynamics model is separated from the topology of the actual track. Compared to the original version, several enhancements are carried out:

- The finite element modelling of the rails is refined.
- The rail cant, i.e. the inclination of the rails with respect to the sleepers, is taken into account. Thereby, vertical and lateral motions of the railhead are no longer decoupled.
- The pads between the sleepers and the rails are modelled by distributed springs and dampers, while in [5] compact elements were used.

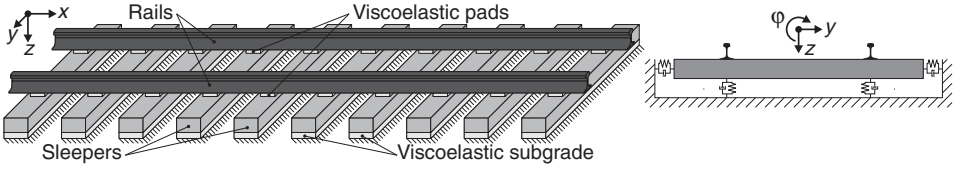

Figure 4. Track models. Left: Detailed model including flexible rails and discrete sleepers. Right: Simple track model for comparison, referenced as 'rigid rails'.

Downloaded by [DLR-Bibliotheken] at 00:15 18 July 2012

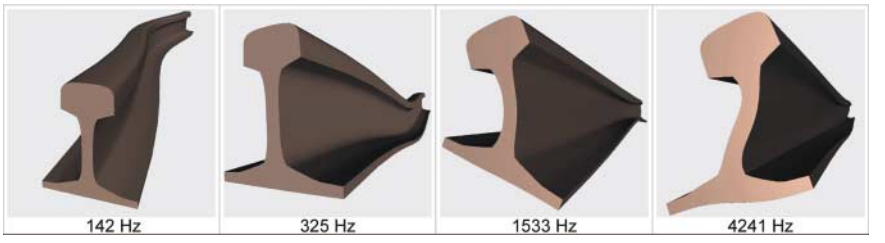

Figure 5. Eigenmodes of the rail having the profile UIC60, wavelength $l_R/c_i = 2.4\,\mathrm{m}$.

The parameters for the sleepers, the pads and the subgrade are taken from [5].

To describe the deformations of the rail, a modal synthesis is used:

$$\mathbf{w}_R(x,y,z,t) = \sum_i \underbrace{\begin{bmatrix} U_i(y,z)\sin(\kappa_i x+\beta_i) \\ V_i(y,z)\cos(\kappa_i x+\beta_i) \\ W_i(y,z)\cos(\kappa_i x+\beta_i) \end{bmatrix}}_{\mathbf{w}_{i,R}(x,y,z)} q_{i,R}(t), \quad \kappa_i = c_i \frac{2\pi}{l_R}, \quad c_i \in \mathbb{Z}. \tag{23}$$

The length of the rail $l_R = n_S \cdot \Delta x_S$ is given by the number of the sleepers n_S and the length of a sleeper span Δx_S. Also in this case, it can be shown that the expression $\mathbf{w} = \mathbf{w}_{i,R}(x,y,z)\cos(\omega_i t)$ is a solution of Navier's equation (10) for a prismatic structure, i.e. for $G = G(y,z)$, $\nu = \nu(y,z)$ and $\rho = \rho(y,z)$ being independent from the longitudinal coordinate x. By using such modes, deformations of the cross-section can be described in addition to the usual deformations such as bending or torsion. Examples of the rail modes are displayed in Figure 5. The shape functions $\mathbf{w}_{i,R}(x,y,z)$ used in the modal synthesis (23) are obtained from a three-dimensional finite element model. Due to the semi-analytic solution, only the cross-section has to be discretised to compute $U_i(y,z)$, $V_i(y,z)$ and $W_i(y,z)$ for a given κ_i.

The question arises, how long the track model has to be given a sufficient approximation for the dynamical behaviour of a very long track. To answer this question, the frequency response function is considered for various numbers of sleepers. The length of the sleeper span is set to $\Delta x_S = 0.6\,\mathrm{m}$, so that the sleeper numbers of $n_S = 16$, $n_S = 32$, $n_S = 64$ and $n_S = 128$ correspond to track lengths of $l_R = 9.6\,\mathrm{m}$, $l_R = 19.2\,\mathrm{m}$, $l_R = 38.4\,\mathrm{m}$ and $l_R = 76.8\,\mathrm{m}$, respectively.

For an excitation by vertical forces, it turns out that a track model including 32 sleepers is sufficient, since the differences to the results obtained with models including 64 or 128 sleepers are very small. However, for the modelling of the lateral vibration behaviour, the convergence is slower, as it can be seen from the results shown in Figure 6. Two different positions of the excitation were used: If the forces act between two sleepers, the pinned–pinned mode of the rail is excited, where the vibration nodes of the rail are located above the sleepers. Therefore, the vibration of the rail is comparatively weakly damped. As a result, a distinct peak occurs at 500 Hz. If the forces act above one sleeper, this peak vanishes. For the case of 16 sleepers, several distinct peaks appear in the range between $f = 200\,\mathrm{Hz}$ and $f = 1500\,\mathrm{Hz}$, which have nearly equal distances. If the number of sleepers is doubled, the peaks are becoming smaller and new peaks occur in the spaces between two existing peaks. These peaks result from waves, which travel through the structure and come back to the point of excitation. In a calculation, which is not shown here, internal damping of the rails was introduced. This leads to a decrease in the peaks, which indicates that the peaks are related to structural vibrations of the rail. These vibrations hardly affect the rail foot, so that only very small motions of the pads, which mainly contribute to the damping, occur. Although even the frequency response function obtained for 128 sleepers still shows small peaks caused by the

Downloaded by [DLR-Bibliotheken] at 00:15 18 July 2012

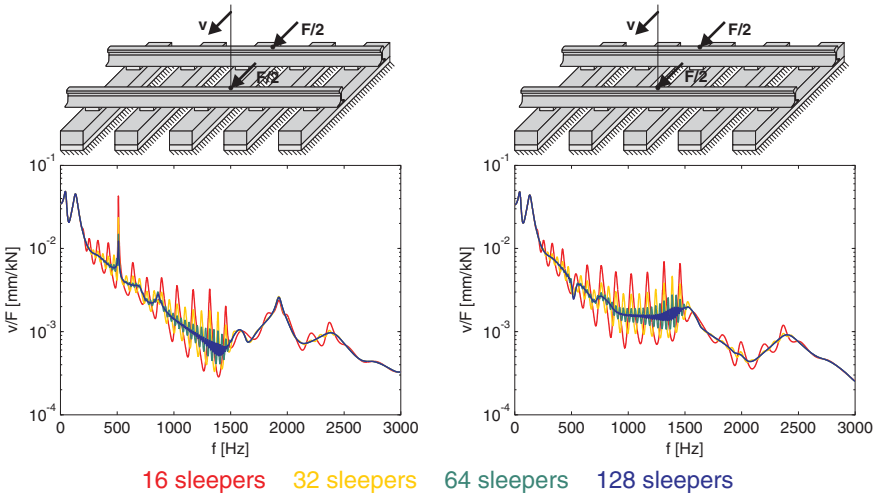

Figure 6. Frequency response function for antimetric lateral excitation between two sleepers (left) and above one sleeper (right).

waves coming back to the point of excitation, this number corresponding to a track length of $l_{\mathrm{R}} = 76.8\,\mathrm{m}$ is chosen.

2.3. *Wheel–rail contact model*

From the view of multi-body dynamics, the wheel–rail contact is a force element, i.e. its input and output are the relative kinematics between wheel and rail and the forces and torques acting between these two bodies, respectively. These forces are related to the deformations of the two bodies in the contact zone compensating the interpenetrations, which would occur if the two surfaces would stay undeformed. These deformations occur in the actual contact patch and in its immediate neighbourhood, i.e. in a small region compared to the main dimensions of the wheel and the rail. Therefore, for further considerations the deformations are split into local deformations, i.e. deformations in and around the contact, and global deformations, e.g. bending or torsion concerning the whole structure.

For the determination of the contact area and the stress distributions, the Hertzian theory is widely used. Here, it is assumed that the contact area is an ellipse and that the distribution of the normal pressure is an ellipsoid. Since an ellipse can be described by its semiaxes, i.e. by two parameters, the Hertzian theory uses tables for the coefficients, which enables very fast calculations. Also, Kalker's linear theory and the FASTSIM algorithm by Kalker, see [7], are based on elliptical contact areas. However, for some wheel–rail profile combinations non-elliptic contact patches occur, since some rail profiles like UIC60 show abrupt changes of the curvature. There are several possibilities to solve this problem.

- Equivalent ellipses: The non-elliptic contact patch is replaced by an elliptic one, which leads to the same contact forces.
- Estimation of the contact area: Several characteristics of the Hertzian contact are applied to the non-elliptic contact to estimate the contact patch and the stresses based on the geometrical interpenetration. A survey of these methods is given by Piotrowski and Chollet in [8].

Downloaded by [DLR-Bibliotheken] at 00:15 18 July 2012

- Solution of the contact equations: A relation between the contact stresses and the deformations is formulated. For the non-elliptic case, this usually requires a discretisation of the problem. Two possibilities are:
  (a) Finite element method (FEM).
  (b) Boundary element method (BEM).

It is obvious that the solution of the contact equations requires the highest numerical effort. Today, the performance of computers allows integration of the iterative solution of the contact problem into an MBS simulation.

For the wheel–rail contact used here, the BEM is chosen, since it seems to be a good compromise between accuracy and computational efficiency. The fundamentals are given by Kalker in [7]. For the BEM solution, on which the well-known program CONTACT by Kalker is based, the equations of Boussinesq and Cerrutti are used. If the material parameters, i.e. the shear modulus G and Poisson's ratio ν, are equal for both halfspaces, the relation between the normal pressure p and the normal deformation w is decoupled from the relation between the tangential stresses τ_1 and τ_2 and the tangential deformations u_1 and u_2. Therefore, the normal contact problem can be solved first. The relation between the pressure distribution $p(x, y)$ and the normal deformation $w(X, Y)$ at the surface is given by

$$w(X,Y) = \frac{1-\nu}{\pi\, G} \int_A \frac{p(x,y)}{R}\, \mathrm{d}A, \quad R = \sqrt{(X-x)^2 + (Y-y)^2}. \tag{24}$$

Here, $w(X, Y)$ represents the resulting deformation of both bodies. For a tangential stress field described by $\tau_1(x, y)$ and $\tau_2(x, y)$, the tangential deformations $u_1(X, Y)$ and $u_2(X, Y)$ at the surface are given by

$$u_1(X,Y) = \frac{1}{\pi\, G} \int_A \left[\frac{1-\nu}{R} + \frac{(X-x)^2 \nu}{R^3} \right] \tau_1(x,y)\, \mathrm{d}A + \frac{\nu}{\pi\, G} \int_A \frac{(X-x)(Y-y)}{R^3} \tau_2(x,y)\, \mathrm{d}A, \tag{25}$$

$$u_2(X,Y) = \frac{\nu}{\pi\, G} \int_A \frac{(X-x)(Y-y)}{R^3} \tau_1(x,y)\, \mathrm{d}A + \frac{1}{\pi\, G} \int_A \left[\frac{1-\nu}{R} + \frac{(Y-y)^2 \nu}{R^3} \right] \tau_2(x,y)\, \mathrm{d}A. \tag{26}$$

The indices 1 and 2 denote stresses and deformations in the longitudinal and the lateral direction, respectively. Also in this case, the deformations u_1 and u_2 denote the resulting deformation of both bodies. To discretise the problem, a grid is defined using a spacing of Δa in both directions, so that the deformations at the grid points are given by

$$\begin{aligned} & x_i = n_{x,i} \Delta a,\ y_i = n_{y,i} \Delta a,\ n_{x,i}, n_{y,i} \in \mathbb{Z} \\ & \quad \Rightarrow u_{1,i} = u_1(x_i, y_i), u_{2,i} = u_2(x_i, y_i), w_i = w(x_i, y_i). \end{aligned} \tag{27}$$

The distributions of the stresses are discretised by using local bilinear functions $f_k(x, y)$ as shown in Figure 7, which are scaled with the values $\tau_1(x_k, y_k)$, $\tau_2(x_k, y_k)$ and $p(x_k, y_k)$ of the stresses at the grid points:

$$\begin{bmatrix} \tau_1(x,y) \\ \tau_2(x,y) \\ p(x,y) \end{bmatrix} = \sum_k \begin{bmatrix} \tau_1(x_k,y_k) \\ \tau_2(x_k,y_k) \\ p(x_k,y_k) \end{bmatrix} f_k(x,y) = \sum_k \begin{bmatrix} \tau_{1,k} \\ \tau_{2,k} \\ p_k \end{bmatrix} f_k(x,y). \tag{28}$$

Inserting the discretised stresses into the Boussinesq–Cerrutti equations leads to the following systems of linear equations:

$$\mathbf{H}_{33}\mathbf{p} = \mathbf{w}, \begin{bmatrix} \mathbf{H}_{11} & \mathbf{H}_{12} \\ \mathbf{H}_{12} & \mathbf{H}_{22} \end{bmatrix} \begin{bmatrix} \mathbf{t}_1 \\ \mathbf{t}_2 \end{bmatrix} = \begin{bmatrix} \mathbf{u}_1 \\ \mathbf{u}_2 \end{bmatrix}. \tag{29}$$

Downloaded by [DLR-Bibliotheken] at 00:15 18 July 2012

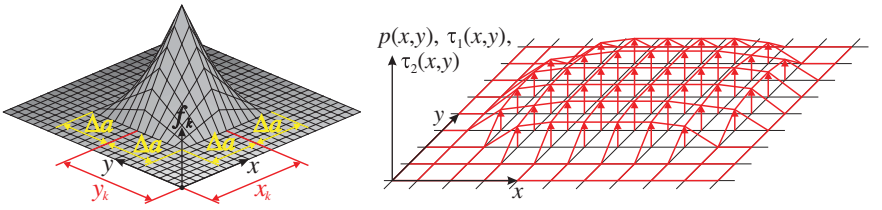

Figure 7. Local bilinear function f_k (left), discretisation of the distribution of the stresses (right).

The vectors $\mathbf{t}_1$, $\mathbf{t}_2$ and $\mathbf{p}$ contain the stresses $\tau_{1,k}$, $\tau_{2,k}$ and p_k and the vectors $\mathbf{u}_1$, $\mathbf{u}_2$ and $\mathbf{w}$ the deformations $u_{1,i}$, $u_{2,i}$ and w_i, respectively.

For the solution of the normal contact problem, the interpenetrations $\delta_i = \delta(x_i, y_i)$ of the undeformed surfaces of wheel and rail at the gridpoints are determined. The conditions for the solutions are given by

$$\text{inside the contact area} : \delta(x_i, y_i) - w(x_i, y_i) = 0 \wedge p(x_i, y_i) > 0, \tag{30}$$

$$\text{outside the contact area} : \delta(x_i, y_i) - w(x_i, y_i) < 0 \wedge p(x_i, y_i) = 0. \tag{31}$$

The condition that the pressure cannot be negative makes the solution of the system of linear equations difficult: At the start of the calculation, it is not known, at which points the pressure is positive and thereby of how many equations the system consists. An efficient way of solving this problem is the Gauss–Seidel method, which had already been presented by Vollebregt for contact problems in [9]. The i-th equation of the normal contact problem $\mathbf{H}_{33}\,\mathbf{p} = \mathbf{w}$ is transformed into an iterative scheme:

$$\sum_{j=1}^{n} H_{ij}^{(33)} p_j = \delta_i \Rightarrow p_i^{(k+1)} = \frac{1}{H_{ii}^{(33)}} \left[\delta_i - \sum_{j=1}^{i-1} H_{ij}^{(33)} p_j^{(k+1)} - \sum_{j=i+1}^{n} H_{ij}^{(33)} p_j^{(k)} \right]. \tag{32}$$

Here, $p_j^{(k)}$ denotes the k-th approximation for the pressure p_j. The nonlinear condition can be easily taken into account by setting $p_i^{(k+1)} = 0$ if the iteration (32) yields a negative value for $p_i^{(k+1)}$.

For the solution of the tangential contact problem, the relative velocities in the contact are considered, which are given for both directions by

$$v_I(x, y) = v_{I,0}(x, y) + v_{I,\mathrm{def}}(x, y) \approx v_{I,0}(x, y) + \frac{u_I(x, y) - u_I^*(x, y)}{\Delta t}, \quad I = 1, 2. \tag{33}$$

Here, $v_{I,0}$ denotes the relative velocity of the entire bodies, while $v_{I,\mathrm{def}}$ describes the velocity due to deformations. This velocities can be approximated by using the deformation $u_I(x, y) = u_I(x, y, t_0)$ at the current time t_0 and the deformation $u_I^*(x, y) = u_I(x, y, t_0 - \Delta t)$ at an earlier time. In the case of adhesion, the relative velocities in the contact vanish, i.e. $v_1(x, y) = 0$ and $v_2(x, y) = 0$. This leads to the conditions:

$$u_I(x, y) = u_I^*(x, y) - \Delta t \cdot v_{I,0}(x, y), \quad I = 1, 2. \tag{34}$$

By applying these conditions to the right-hand side of the system (28) and transforming the equations into a form analogous to (32), new approximations $\tau_1^{(k+1)}(x, y)$ and $\tau_2^{(k+1)}(x, y)$ for the tangential stresses are obtained. However, the transmittable tangential stress is limited by the pressure $p(x, y)$ at the considered point and the friction coefficient μ, i.e. $\sqrt{\tau_1(x, y)^2 + \tau_2(x, y)^2} = |\tau(x, y)| \leq \mu\, p(x, y)$. Therefore, it has to be checked, whether the

Downloaded by [DLR-Bibliotheken] at 00:15 18 July 2012

resulting stress $|\tau^{(k+1)}(x,y)|$ is smaller than the transmittable stress. If the approximation exceeds the transmittable stress $\mu p(x,y)$, this indicates sliding. In this case, the tangential stress acts in the opposite direction to the relative velocity, which leads to the following condition:

$$\begin{bmatrix}\tau_1(x,y)\\ \tau_2(x,y)\end{bmatrix} = -C\begin{bmatrix}v_1(x,y)\\ v_2(x,y)\end{bmatrix}, \quad C > 0 \Rightarrow \tau_1(x,y)v_2(x,y) - \tau_2(x,y)v_1(x,y) = 0. \tag{35}$$

Furthermore, the resulting tangential stress has to be equal to the transmittable stress, i.e. $\sqrt{\tau_1(x,y)^2 + \tau_2(x,y)^2} = \mu p(x,y)$. Due to this nonlinear condition, the Gauss–Seidel method provides also in this case an efficient way to solve the system of equations, as presented by Vollebregt in [9].

For the wheel–rail contact model presented here, stationary rolling is assumed. The particles move through the contact in negative x-direction. If a time interval of $\Delta t = \Delta a/v_0$ is chosen, the deformation $u_I^*(x,y)$ can be set to $u_I^*(x,y) = u_I(x - \Delta a, y)$, i.e. in the stationary case the earlier deformation of the particle, which is currently considered, is equal to the deformation of the next particle.

Downloaded by [DLR-Bibliotheken] at 00:15 18 July 2012

3. Calculation results

To investigate the behaviour of the refined vehicle–track model, two scenarios are studied: The centred running and the permanent hunting, which occurs if the vehicle runs faster than the critical speed. In both cases, the track is straight and no track disturbances are taken into account. It can be objected that these scenarios are very idealised ones, since in real-life track disturbances always occur and since the permanent hunting is also usually avoided. However, these scenarios can serve as a verification of the model. The investigation of the permanent hunting also is useful, because here the contact patch moves through wide ranges of the profiles of wheel and rail.

To study the influences, which the flexibilities of the wheelsets and of the track have on the running behaviour, four configurations of the vehicle–track model are considered. For the sake of brevity, the following abbreviations will be used:

- RR: rigid wheelsets, rigid rails.
- FR: flexible wheelsets, rigid rails.
- RF: rigid wheelsets, flexible rails.
- FF: flexible wheelsets, flexible rails.

For the case of 'rigid rails', the simple track model shown in Figure 4 is used.

All results presented in the following refer to the leading wheelset of the leading bogie. Generally, the profiles S1002 and UIC60 are used for the wheels and the rails, respectively. A value of 1/40 is set for the rail cant. For the wheel–rail contact, the friction coefficient is set to $\mu = 0.3$ and a spacing of $\Delta a = 0.75$ mm is used.

3.1. *Centred running*

For the centred running, a running speed of $v_0 = 200$ km/h is set. The results are displayed in Figures 8–11. The vertical forces acting on the wheel rim and on the journals of the wheelset cause a bending of the axle and thereby a positive camber angle of the wheels, as displayed in Figure 12. This change of the inclination of the wheel rim relative to the rail head is very small: For the rigid wheelset on rigid rails, the angle is 25 mrad, i.e. the cant of the rail.

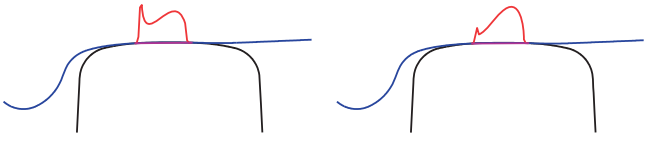

Figure 8. Contact geometry; left: model RR, right: model FF.

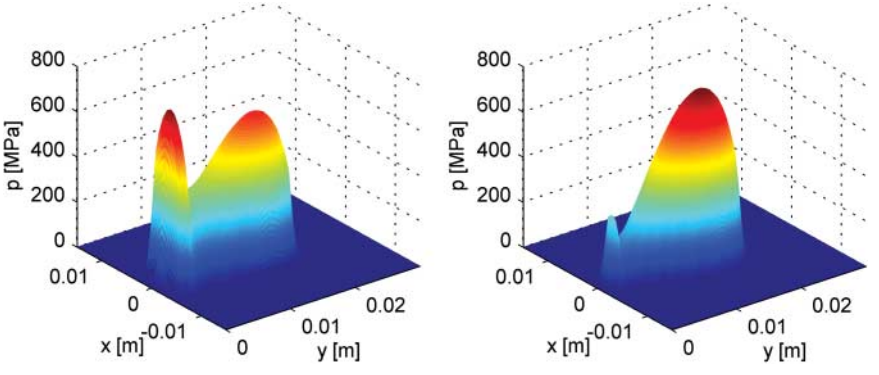

Figure 9. Distribution of the normal pressure; left: model RR, right: model FF.

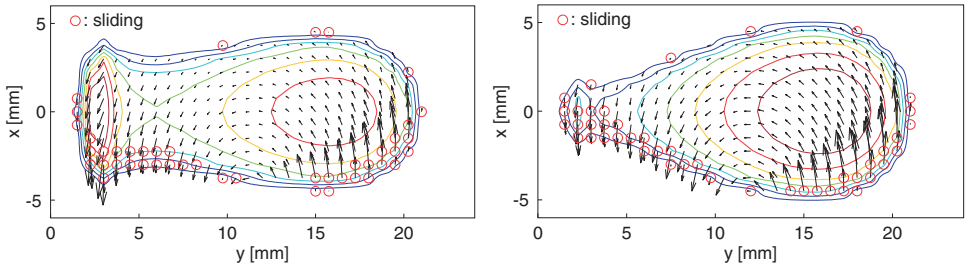

Figure 10. Distribution of the tangential stresses; left: model RR, right: model FF.

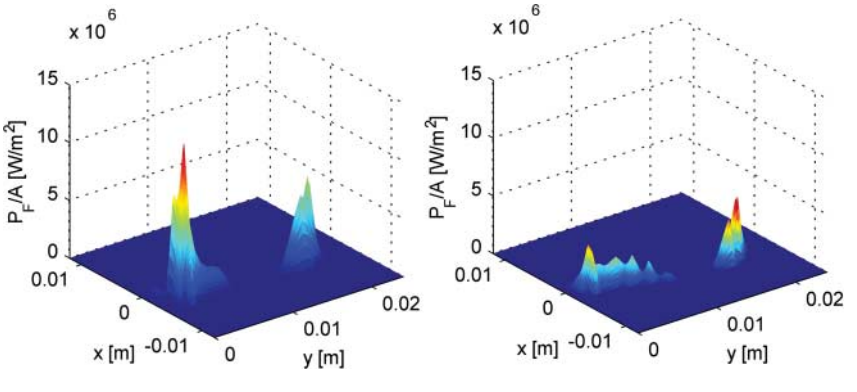

Figure 11. Distribution of the frictional power density; left: model RR, right: model FF.

In the case of flexible wheelsets on flexible rails, the angle is ≈ 26 mrad, so the change of the contact geometry is hardly visible, see Figure 8. However, the impact on the contact is considerable: The left maximum of the pressure distribution, which occurs for the RR model,

Downloaded by [DLR-Bibliotheken] at 00:15 18 July 2012

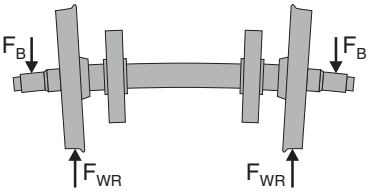

Figure 12. Qualitative scheme of the bending of the wheelset due to the forces acting at the wheel rims (F_{WR}) and at the journals (F_{B}).

shrinks drastically for the FF model and nearly vanishes. The creepages occurring in the contact are caused by the spin due to the inclination of the contact patch relative to the axle of the wheelset. The concentric pattern of the tangential stresses due to the spin is clearly visible in Figure 10. The sliding occurs at the trailing edge of the contact patch, the few single points of sliding at the leading edge result from discretisation errors. In Figure 11 it can be seen that the deformations have a strong impact on the distribution of the frictional power density, which is relevant for wear: For the model RR, a maximum of $P_F/A = 13\,\mathrm{W/mm^2}$ is observed in the left part of the contact patch, and a further local maximum of $P_F/A = 7\,\mathrm{W/mm^2}$ occurs in the right part. For the model FF, the right maximum is slightly reduced to $P_F/A = 5\,\mathrm{W/mm^2}$, while the left maximum shrinks drastically to $P_F/A = 4\,\mathrm{W/mm^2}$, because due to the reduced pressure p in this region the transmittable tangential stress $\tau_{\max} = \mu\, p$ is also smaller.

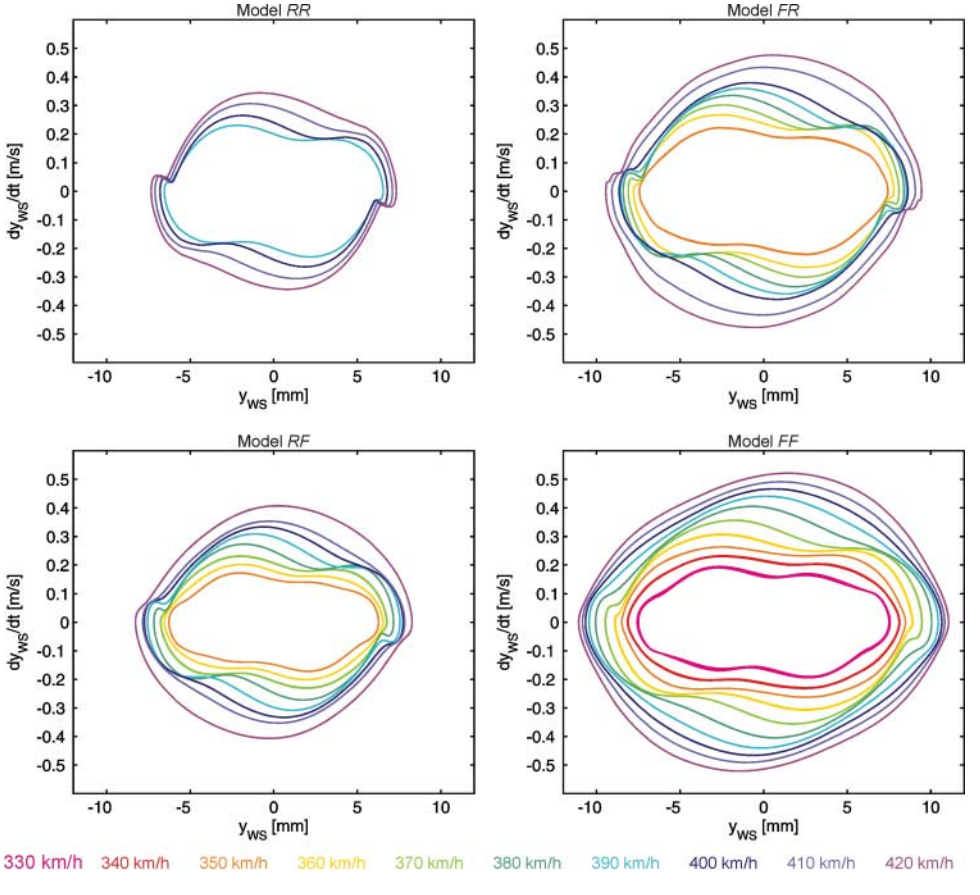

Figure 13. Phase portraits for the lateral displacement y_{WS} of the wheelset's centre.

Downloaded by [DLR-Bibliotheken] at 00:15 18 July 2012

3.2. *Hunting behaviour*

If the vehicle runs faster than the so-called critical speed, the hunting motions do not die out, but a permanent hunting occurs. This scenario is investigated for the four configurations of the vehicle–track model. In Figure 13, the phase portraits for the lateral displacement y_{WS} at the wheelset's centre are displayed. Comparing the phase plots, three main differences can be seen:

- The amplitudes are larger, if the flexibility is taken into account. Especially, the flexibility of the wheelset leads to a distinct increase in the wheelset's motion. If the flange hits the rail head, the wheel rim is deformed towards the centre of the wheelset. This causes a larger lateral displacement of the wheelset's centre.
- In the diagram for the variant RR, sharp bends of the curves can be seen at $y_{WS} \approx 7$ mm and $y_{WS} \approx -7$ mm. This sharp bend results from the wheel flange hitting the rail head. In the other diagrams, the curves are smoother. The wheelset and the rail are softer than the comparatively stiff wheel–rail contact, so that the flexibilities are cushioning the impact. Especially, the support of the rails by the pads leads to a 'milder' impact than in the case of the collision with the rigid body of the track element.
- The curves for $v_0 = 330$ km/h and $v_0 = 340$ km/h are missing for the configurations FR and RF, and for the configuration RR the curves from $v_0 = 330$ km/h up to $v_0 = 380$ km/h are missing, because for these configurations no permanent hunting occurs at these running speeds. This indicates that the structural flexibilities cause a lower critical speed.

The wheel–rail contact geometry and the position of the contact patch are displayed in Figure 14. For the model RR, the figures for $y_{WS} = 9$ mm and $y_{WS} = 11$ mm are missing, since

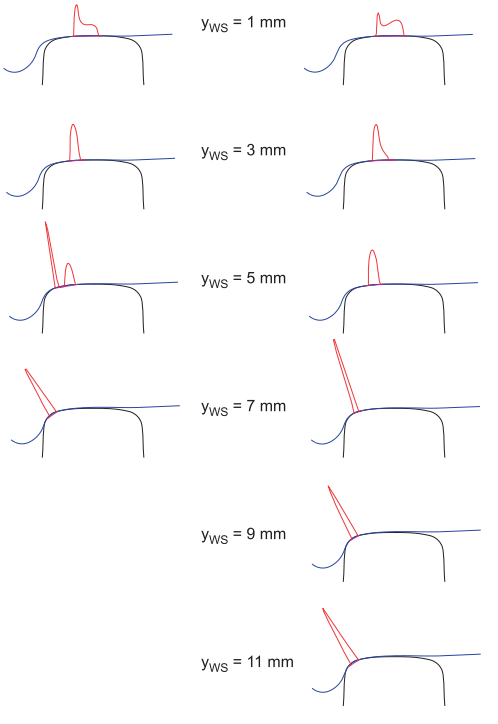

Figure 14. Contact geometry and normal pressure distribution depending on the lateral displacement y_{WS} of the wheelset's centre.

Downloaded by [DLR-Bibliotheken] at 00:15 18 July 2012

the lateral displacement does not reach a value of $y_{WS} = 8\,\text{mm}$. It can also be seen that for the displacements of $y_{WS} = 9\,\text{mm}$ and $y_{WS} = 11\,\text{mm}$, the position of the contact patch hardly changes. This supports the thesis that the displacement is caused by structural deformations of the wheelset and the track.

4. Conclusions

Even in the 'unspectacular' case of centred running, the influence of the structural deformations is visible. For the permanent hunting, the structural deformations have a strong impact on the contact and thereby on the running behaviour of the entire vehicle: The critical speed is shifted to lower values, and the shape of the motion itself distinctly changes. The investigation of the separate influences of the flexibility of the wheelset and the flexibility of the track shows that both have a significant impact on the running behaviour: The flexibility of the wheelset leads to a larger increase in the lateral displacement and the flexibility of the track has a more distinctive cushioning effect.

The observation that structural deformations have an impact on the stress distributions occurring in the wheel–rail contact underlines the importance of consistent modelling, i.e. for a refined modelling of the vehicle–track interaction the key components should have a similar modelling depth. Of course, a more detailed model of the wheel–rail contact requires a far higher computational effort than a simple one. However, this increased effort is only sensible, if the inputs of the contact module also come from more detailed models.

The refined model including rotating flexible wheelsets, discretely supported flexible rails and a detailed wheel–rail contact model can be used as a base for further investigations concerning noise and wear. Since the accuracy of results depends not only on the model, but also on the input parameters, an extension of the model to realistic track disturbances and the application of realistic profiles, i.e. measured worn profiles instead of the shapes defined in the standards, are desirable.

References

[1] P. Diepen, *Horizontaldynamik von Drehgestellfahrzeugen: Berechnung und Optimierung des Laufverhaltens von schnellfahrenden Reisezugwagen mit konventionellen Laufwerken*, dissertation, TU Braunschweig, Germany, 1991.

[2] K.H. Kim, *Verschleissgesetz des Rad-Schiene-systems*, dissertation, RWTH Aachen, Germany, 1996.

[3] L. Landau and E. Lifshitz, *Theory of Elasticity*, Butterworth-Heinemann, Oxford, 1986.

[4] I. Kaiser, A. Heckmann, and F.v.d. Linden, *On an ALE-approach for rotating elastic structures*, Multibody Dynamics 2007, ECCOMAS Thematic Conference, Milano, Italy, 25–28 June 2007.

[5] B. Ripke, *Hochfrequente Gleismodellierung und Simulation der Fahrzeug-Gleis-Dynamik unter Verwendung einer nichtlinearen Kontaktmechanik*, Fortschritt-Berichte Reihe 12 VDI-Verlag, Duesseldorf, 1995.

[6] H. Netter, *Rad-Schiene-Systeme in Differential-Algebraischer Darstellung*, Fortschritt-Berichte Reihe 12 VDI-Verlag, Duesseldorf, 1998.

[7] J.J. Kalker, *Three-Dimensional Elastic Bodies in Rolling Contact*, Kluwer Academic Publishers, Dordrecht, 1990.

[8] J. Piotrowski and H. Chollet, *Wheel–rail contact models for vehicle system dynamics including multi-point contact*, Veh. Syst. Dyn. 43 (2005), pp. 455–483.

[9] E.A.H. Vollebregt, *A Gauss–Seidel type solver for special convex programs, with application to frictional contact mechanics*, J. Optim. Theory Appl. 87 (1995), pp. 47–67.

Downloaded by [DLR-Bibliotheken] at 00:15 18 July 2012